Amplitude-Phase Detection for Power Converters Tied to Unbalanced Grids with Large X/R Ratios

Liansong Xiong, *Senior Member, IEEE,* Xiaokang Liu, *Member, IEEE,*
Lei Liu, and Yonghui Liu, *Student Member, IEEE*

***Abstract*—Amplitude-phase information of the voltage/current phasor, which is the prerequisite for grid-tied converter control and protection, can change almost instantaneously in low-voltage distribution systems with small X/R ratios. However, the equivalent impedances of high-voltage power systems are usually inductive (with large X/R ratios), and the power flow of pertinent grids generates decaying DC (DDC) components with large amplitude and long duration during large disturbances. Therefore, the X/R ratios and DDC components must be fully considered in amplitude-phase detection to achieve effective converter control and protection. To this end, the main components present in the transient voltage/current of a high-voltage power system after unbalanced disturbance are first analyzed, and the general transient model is obtained by synthesizing multi-mode DDC components. Then, by resorting to waveform characteristics of different components, an amplitude-phase detection algorithm is proposed based on the multi-component parallel-detection structure. Compared to existing techniques, the detection time is reduced to half grid cycle. Finally, an iterative variable-interval integral algorithm is developed, improving the anti-noise ability of detection algorithm, and overcoming the computational burden issue. This enables the direct integration of algorithm into the converter's embedded processor. Experiment results verified the effectiveness and superiority of the proposed technique.**

***Index Terms*—Amplitude-phase detection, X/R ratio, decaying DC component, unbalanced disturbance.**

I. Introduction

For high-voltage overhead lines, high power generators, large transformers, and distribution networks with large inductive loads, the equivalent impedances are generally dominated by inductive components (i.e., their X/R ratios are large), and the time constants of equivalent circuits are significant. After major disturbances (e.g., faults and large load switching), electrical quantities such as the grid voltage and current will inevitably exhibit decaying DC (DDC) components with large amplitude and long duration during transient. These DDC components have a significant impact on several important links in the power grid [1]–[3], encompassing amplitude-phase detection, fault identification and location, fault ride-through control, and protection device activation.

Among them, fast and accurate amplitude-phase detection is the basis for the subsequent works [4], and is crucial for high-performance control of converters [5], [6]. Indeed, with the wide application of converters, the grid code requires grid-tied converters to equip with fault ride-through capabilities [7]–[9], making it necessary to study effective amplitude-phase detection methods when considering DDC components associated with large grid X/R ratios. However, the majority of existing detection methods for the application scenario of converter control and protection assume that the amplitude and phase of the grid voltage and current can change instantaneously during large disturbances, and that the transient process is negligible. Indeed, these assumptions are reasonable merely for grids with small X/R ratios.

Concerning the impact of large DDC components, instead of amplitude-phase detection, the existing works mainly focus on multiple application scenarios such as grid fault analysis, fault location, and relay protection strategies [10]. These works provide insightful information on two critical aspects for developing amplitude-phase detection schemes, namely, analytical tools for mechanism analysis, and practical DDC detection methods.

Previous works investigated the mechanism of DDC components and their possible impact on the grid voltage/current phasor, especially when considering large X/R ratios of power systems. In [11], by considering the voltage and current cannot change instantaneously in a grid with numerous transmission lines, generators and transformers that are highly inductive, it is proved that the existence of DDC component is inevitable. The magnitude and duration time of the DDC component are determined by the X/R ratio of transient circuit and the grid voltage at the transient beginning [12]. In the worst scenario, the peak value of the transient current, when accounting for the contribution of DDC components, approaches twice that of the steady-state current [13], severely jeopardizing the safety and stability of the utility grid and converters. However, to the best of the Authors' knowledge, no literature work investigated the mechanism for multiple DDC components during the transient, or the relationship between DDC components and sequence components. In-depth research is still needed for modeling transient electrical characteristics of high-voltage power grids after their being disturbed.

To annihilate the DDC interference on grid amplitude-phase detection, DDC components must be accurately and timely detected. Indeed, the DDC component detection methods have

Manuscript received May 11, 2021; revised July 26, 2021; accepted August 10, 2021. This work was supported in part by the National Natural Science Foundation of China (51707091), and in part by the Key Laboratory of Control of Power Transmission and Conversion (SJTU), Ministry of Education (2018AC04). *(Corresponding author: Xiaokang Liu.)*

L. Xiong is with the School of Automation, Nanjing Institute of Technology, Nanjing 211167, China and also with the Key Laboratory of Control of Power Transmission and Conversion, Shanghai Jiao Tong University, Shanghai 200240, China, (e-mail: xiongliansong@163.com).

X. Liu is with the Department of Electronics, Information and Bio-engineering, Politecnico di Milano, 20133 Milano, Italy (e-mail: xiaokang.liu@polimi.it).

L. Liu and Y. Liu are with the School of Electrical Engineering, XJTU (e-mail: leiliuxjtu@stu.xjtu.edu.cn; liuyonghui@stu.xjtu.edu.cn).

been intensively investigated during the last few years. In [13], the empirical mode decomposition with Hilbert transform has been used for phasor estimation and takes 2.25 grid cycles to estimate the DDC components. The method in [12] can reduce the convergence time to about 1 grid cycle with a time constant of 200 ms. However, this algorithm needs to solve nonlinear minimization problems and therefore has a large computational burden. To implement the DDC detection in the embedded controller of power converters, the improved DFT algorithm in [14] provides lower computational complexity and shorter execution time. However, the estimated magnitude has certain error and fluctuates for several grid cycles. In [2], the active power filter fails to prevent the maximum impact current polluting the utility grid when the detection of fundamental AC component takes 1 grid cycle. Via the mathematical morphology method [15], the DDC components can be extracted in more than 0.5 grid cycle. However, this method only outputs multi-step values (with each step being 0.5 grid cycle) yet cannot track the real-time DDC components continuously. The Volterrra least mean square/fourth filter [16] can accurately estimate the DDC components in the presence of white noise. However, it requires complicated parameter tuning to obtain accurate results and a desired response time longer than 1 grid cycle.

When focusing on the application scenario of amplitude-phase detection for grid-connected converters, and considering the large impact of DDC components, the following concerns should be taken into account:

- The embedded controller of the converter, usually a digital signal processor (DSP), has limited computing power, restricting the computational complexity and amount of the amplitude-phase detection algorithm. From the perspective of fault cause analysis and location, it is necessary to extract the characteristic parameters of each DDC component separately [17], inevitably requiring huge mathematical operations. However, from the perspectives of disturbance suppression, fault ride-through, and safety protection, the converter system needs to consider merely the comprehensive effect of multiple DDC components that act simultaneously, without focusing on each component and its characteristic parameters.
- The overload capacity of the converter is relatively weak, and long-term overloading will cause device performance decline [18] or even damage [19]. Hence, it is critical to timely detect the main components of the transient, and provide necessary amplitude-phase information for the converter control and protection [20]. This lays the foundation of fast and effective disturbance suppression, fault ride-through and safety protection, and effectively limits the transient impact (in terms of both duration and intensity) on the converter.

To this end, this paper analyzes the transient electrical characteristics of the high-voltage power grid after large disturbance, and synthesizes multi-mode DDC components into an equivalent one. Then, amplitude-phase detection is realized by developing a multi-component parallel-detection structure. This method allows to detect grid components simultaneously in the presence of DDC transients. Compared to the existing techniques, the detection time of proposed method is reduced to half grid cycle.

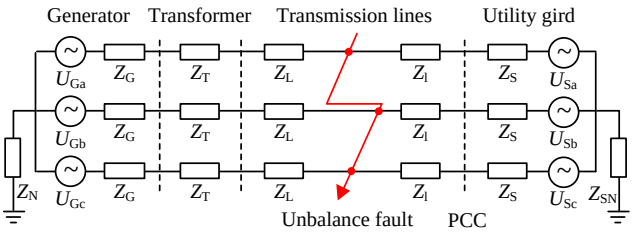

Fig. 1. Equivalent circuit diagram of a typical high-voltage power system.

II. Negative Effect of Large X/R Ratios of High Voltage Power Systems

In areas with abundant electric energy resources that cannot be fully utilized locally, high-voltage overhead lines of hundreds of kilovolts are normally necessary to transmit the electricity to load centers at least 100 km away. As shown in Fig. 1, a typical high-voltage power transmission system comprises a power plant, a step-up transformer, high-voltage transmission lines, and a utility grid connecting external power sources via the point of common coupling (PCC). Here, $\mathbf{U}_{\mathrm{G}}$, $\mathbf{Z}_{\mathrm{G}}$, and $\mathbf{Z}_{\mathrm{N}}$ are the electromotive force, internal impedance, and neutral-ground impedance vectors of the power plant; $\mathbf{Z}_{\mathrm{T}}$ is the impedance vector of step-up transformer; $\mathbf{Z}_{\mathrm{L}}$ and $\mathbf{Z}_{\mathrm{l}}$ are the impedance vectors of transmission lines on the left and right sides of the disturbance point; $\mathbf{U}_{\mathrm{S}}$, $\mathbf{Z}_{\mathrm{S}}$, and $\mathbf{Z}_{\mathrm{SN}}$ are the electromotive force, internal impedance and neutral-ground impedance vectors of the utility grid in the Thevenin equivalent circuit.

Due to long-term exposure and large spatial span, high-voltage overhead lines are extremely susceptible to various external disturbances. By considering an asymmetric fault example of transmission lines with reference to Fig. 1, and by solving the time-domain expressions of the line current and PCC voltage during the transient, the influential law of the X/R ratio on the system transient features is illustrated in this manuscript.

To facilitate the derivation of line current expression during the transient, a three-phase voltage source $\mathbf{U}_{\mathrm{F}}$ is used to represent the steady-state asymmetric voltage at the disturbance point (see Fig. 2 for the simplified circuit). Accordingly, the total system voltage $\mathbf{U}$ in Fig. 2 is given by

$$\mathbf{U} = \mathbf{U}_{\mathrm{G}} - \mathbf{U}_{\mathrm{F}} = \mathbf{U}^{+} + \mathbf{U}^{-} + \mathbf{U}^{0} \tag{1}$$

where

$$\mathbf{U} = \begin{bmatrix} u_a & u_b & u_c \end{bmatrix}^{\mathrm{T}}, \mathbf{U}^{+} = \begin{bmatrix} u_a^{+} & u_b^{+} & u_c^{+} \end{bmatrix}^{\mathrm{T}}$$
$$\mathbf{U}^{-} = \begin{bmatrix} u_a^{-} & u_b^{-} & u_c^{-} \end{bmatrix}^{\mathrm{T}}, \mathbf{U}^{0} = \begin{bmatrix} u_a^{0} & u_b^{0} & u_c^{0} \end{bmatrix}^{\mathrm{T}}$$

Afterward, the asymmetric system in Fig. 2 is decomposed into positive-, negative-, and zero-sequence circuits. Specifically, the sequence circuits of phase a are shown in Fig. 3, where Z_{G}^{+}, Z_{G}^{-}, and Z_{G}^{0} are the positive-, negative-, and zero-sequence impedances of the generator, respectively; Z_{T}^{+},

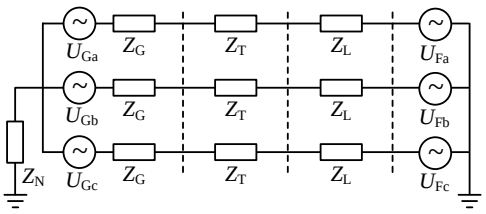

Fig. 2. Simplified equivalent circuit of the studied system after disturbance.

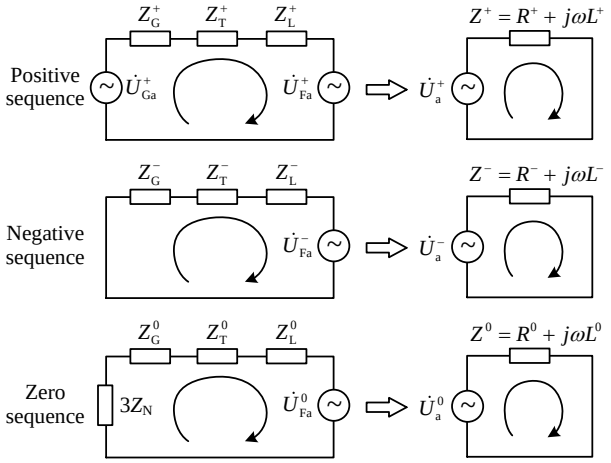

Fig. 3. Sequence equivalent circuits of the disturbed system (phase a).

Z_{T}^-, and Z_{T}^0 are the positive-, negative-, and zero-sequence impedances of the transformer, respectively; Z_{L}^+, Z_{L}^-, and Z_{L}^0 are the positive-, negative-, and zero-sequence impedances of the transmission lines, respectively; R^+, R^-, and R^0 are the equivalent resistances of the positive-, negative-, and zero-sequence circuits, respectively; L^+, L^-, and L^0 are the equivalent inductances of the positive-, negative-, and zero-sequence circuits, respectively.

For ease of representation, let the disturbance time be $t = 0$. Assume the line current to be I at the disturbance instant, and the steady-state current phases of positive-, negative-, and zero-sequence circuits in Fig. 3 to be θ^+, and θ^-, and θ^0, respectively, then the transient currents in positive-, negative-, and zero-sequence circuits of phase a are

$$\begin{cases} i_a^+(t) = I^+ \sin\left(\omega t + \theta^+\right) - \left(I^+ \sin\theta^+ - I\right) e^{-\frac{R^+}{L^+}t} \\ i_a^-(t) = I^- \sin\left(\omega t + \theta^-\right) - I^- \sin\theta^- e^{-\frac{R^-}{L^-}t} \\ i_a^0(t) = I^0 \sin\left(\omega t + \theta^0\right) - I^0 \sin\theta^0 e^{-\frac{R^0}{L^0}t} \end{cases} \tag{2}$$

Accordingly, after the asymmetric disturbance, the transmission line transient current of phase a can be expressed as

$$i_a = i_a^+(t) + i_a^-(t) + i_a^0(t) \tag{3}$$

By considering (with $\boldsymbol{\alpha} = e^{j2\pi/3}$)

$$\begin{bmatrix} \dot{\mathbf{I}}_a \\ \dot{\mathbf{I}}_b \\ \dot{\mathbf{I}}_c \end{bmatrix} = \begin{bmatrix} 1 & 1 & 1 \\ \boldsymbol{\alpha}^2 & \boldsymbol{\alpha} & 1 \\ \boldsymbol{\alpha} & \boldsymbol{\alpha}^2 & 1 \end{bmatrix} \begin{bmatrix} \dot{\mathbf{I}}_a^+ \\ \dot{\mathbf{I}}_a^- \\ \dot{\mathbf{I}}_a^0 \end{bmatrix} \tag{4}$$

the time-domain transient current $\mathbf{I}(t)$ in three-phase transmission lines is expressed as

$$\mathbf{I} = \mathbf{I}^+ + \mathbf{I}^- + \mathbf{I}^0 + \mathbf{I}^{dc} \tag{5}$$

where $\mathbf{I} = \begin{bmatrix} i_a & i_b & i_c \end{bmatrix}^{\mathrm{T}}$

$$\mathbf{I}^+ = \begin{bmatrix} i_a^+ \\ i_b^+ \\ i_c^+ \end{bmatrix} = I^+ \begin{bmatrix} \sin(\omega t + \theta^+) \\ \sin(\omega t + \theta^+ - 2\pi/3) \\ \sin(\omega t + \theta^+ + 2\pi/3) \end{bmatrix}$$

$$\mathbf{I}^- = \begin{bmatrix} i_a^- \\ i_b^- \\ i_c^- \end{bmatrix} = I^- \begin{bmatrix} \sin(\omega t + \theta^-) \\ \sin(\omega t + \theta^- + 2\pi/3) \\ \sin(\omega t + \theta^- - 2\pi/3) \end{bmatrix}$$

$$\mathbf{I}^0 = \begin{bmatrix} i_a^0 \\ i_b^0 \\ i_c^0 \end{bmatrix} = I^0 \begin{bmatrix} \sin\left(\omega t + \theta^0\right) \\ \sin\left(\omega t + \theta^0\right) \\ \sin\left(\omega t + \theta^0\right) \end{bmatrix}$$

and $\mathbf{I}^{dc}$ is given by (6) at the top of next page.

Since it holds that (see Sec. IV-C for proof)

$$\sum_{i=1}^{n} A_i e^{-\sigma_i t} = P(n) = A_n^{\sum} e^{-\sigma_n^{\sum} t} \tag{7}$$

the DDC components given by (6) can be simplified as

$$\mathbf{I}^{dc} = \begin{bmatrix} i_a^{dc} \\ i_b^{dc} \\ i_c^{dc} \end{bmatrix} = \begin{bmatrix} I_a^{dc} e^{-\sigma_a t} \\ I_b^{dc} e^{-\sigma_b t} \\ I_c^{dc} e^{-\sigma_c t} \end{bmatrix} \tag{8}$$

Analogously, according to Kirchhoff's voltage law, the voltage at the PCC in Fig. 1 can be obtained as

$$\mathbf{U}_{\mathrm{PCC}} = \mathbf{U}_{\mathrm{S}} + \mathbf{I}\mathbf{Z}_{\mathrm{S}} = \mathbf{U}_{\mathrm{PCC}}^+ + \mathbf{U}_{\mathrm{PCC}}^- + \mathbf{U}_{\mathrm{PCC}}^0 + \mathbf{U}_{\mathrm{PCC}}^{dc} \tag{9}$$

Based on (5) and (9), in addition to the common positive-, negative-, and zero-sequence components, the decaying DC (DDC) components that gradually decay with time are also present in the line currents and PCC voltages after disturbance.

For low-voltage power distribution systems, the equivalent impedances of power lines and electrical loads are mainly resistive with small X/R ratios, leading to a short duration of the DDC component commonly lasting for a few or a few tens of milliseconds. Besides, the energy transmitted in the distribution lines is low, and the transient impact energy caused by power flow change is also limited, causing a small amplitude of the DDC component. Considering the short duration and small amplitude of the DDC component, the influence of X/R ratio is usually negligible in low-voltage power distribution systems. In such a case, the DDC components in system are considered to be nearly null, and the mutation of state variables (such as voltages and currents) can occur.

However, the impedance of high-voltage overhead lines is usually dominated by inductive components in order to reduce transmission losses. As a matter of fact, the pertinent X/R ratio is usually in the order of hundreds of milliseconds. Indeed, most of the literature adopts pure inductors (with X/R ratio approaching ∞ or R approaching 0) to represent the transmission lines, with the aim of obtaining a concise yet roughly accurate formula for transmitted power. Besides, the equivalent circuits of large generators and transformers are dominated by reactance parameters, and their X/R ratios are

$$\mathbf{I}^{dc}=\begin{bmatrix} i_a^{dc} \\ i_b^{dc} \\ i_c^{dc} \end{bmatrix}=-\begin{bmatrix} \left(I^{+}\sin\theta^{+}-I\right)e^{-\frac{R^{+}}{L^{+}}t}+I^{-}\sin\theta^{-}e^{-\frac{R^{-}}{L^{-}}t}+I^{0}\sin\theta^{0}e^{-\frac{R^{0}}{L^{0}}t} \\ \left[I^{+}\sin\left(\theta^{+}-\frac{2\pi}{3}\right)+\frac{I}{2}\right]e^{-\frac{R^{+}}{L^{+}}t}+I^{-}\sin\left(\theta^{-}+\frac{2\pi}{3}\right)e^{-\frac{R^{-}}{L^{-}}t}+I^{0}\sin\theta^{0}e^{-\frac{R^{0}}{L^{0}}t} \\ \left[I^{+}\sin\left(\theta^{+}+\frac{2\pi}{3}\right)+\frac{I}{2}\right]e^{-\frac{R^{+}}{L^{+}}t}+I^{-}\sin\left(\theta^{-}-\frac{2\pi}{3}\right)e^{-\frac{R^{-}}{L^{-}}t}+I^{0}\sin\theta^{0}e^{-\frac{R^{0}}{L^{0}}t} \end{bmatrix} \tag{6}$$

generally hundreds to thousands of milliseconds. Meanwhile, high-voltage overhead transmission lines, large generators, and transformers transmit huge energy. When they are subjected to major disturbances such as large load switching and short-/open- circuit faults, the system power flow will change significantly, and the substantial energy change inevitably introduces high-amplitude DDC components to system voltages and currents.

Hence, when the power system suffers from a large disturbance or when the X/R ratio of the system equivalent circuit is large, the system voltages and currents exhibit DDC components with large amplitudes and long duration times. In such a case, research works such as system transient analysis, detection, control, and protection need to fully consider the impact of the X/R ratio in the equivalent circuit. The previous assumption, namely, the system voltages, currents, and frequency can change suddenly, is no longer valid.

III. Amplitude-Phase Detection Algorithm

The previous analysis indicates that the X/R ratio of the middle-/high-voltage grid system is relatively large, and the DDC component generated during the transient can no longer be neglected. To investigate on the relevant control and protection of transient features in high-voltage power systems, it is necessary to first detect the voltage/current phasor when the influence of X/R ratio is taken into account.

A. Transient Signal Model Construction

The phasor method is classic for analyzing AC systems operating at base frequency. It neglects the real-time grid frequency that cannot change notably for voltages and currents, and focuses on the amplitude and phase that have larger impact on the system power flow. Hence, it is suitable for analyzing large power systems with virtually undisturbed frequency.

In addition to the inherit assumption of constant grid frequency for the phasor method, several facts also prove that the frequency change can be neglected for the transient feature study of high-voltage power grids. These are

- Unlike low-voltage and small-capacity distribution networks, high-voltage and large-scale power systems do not allow a large frequency deviation or the rate of change of frequency (RoCoF). Grid codes of various countries usually require the steady-state frequency deviation to be within ± 0.2 Hz, and the RoCoF to be within 0.1–1.0 Hz/s [21]. These specifications justify the constant frequency assumption.
- The DDC component only exists in the transient process. Its duration is short w.r.t. the steady-state condition, yet it brings significant transient impact. To mitigate its impact on the system power flow, the pertinent transient control and safety protection should primarily focus on a fast response speed. The accurate frequency detection should be delayed to the steady-state condition where the DDC component is negligible.

Besides, (5) and (9) suggest that the voltages and currents during the grid transient encompass positive-, negative-, and zero-sequence components, as well as DDC components. Accordingly, the transient signal model for deriving the detection algorithm should also include the positive sequence component $\mathbf{X}^{+}$, negative sequence component $\mathbf{X}^{-}$, zero sequence component $\mathbf{X}^{0}$, and DDC component $\mathbf{X}^{dc}$.

Based on these considerations, the amplitude-phase detection algorithm in this manuscript assumes a constant grid frequency ω (equal to synchronous frequency), and extracts the amplitude and phase of the grid phasor $\mathbf{X}$ pertinent to voltages or currents. To this end, $\mathbf{X}$ is expressed in vector form as $\mathbf{X}(t)=\left[x_a(t),x_b(t),x_c(t)\right]^{\mathrm{T}}$, and (with X^{+}, X^{-}, and X^{0} being positive-, negative-, and zero-sequence amplitudes, respectively; θ^{+}, θ^{-}, and θ^{0} being positive-, negative-, and zero-sequence initial phases, respectively; X_k^{dc} and σ_k being the amplitude and decaying coefficient of the DDC component in phase k, respectively, and $k=a,b,c$):

$$\mathbf{X}(t)=\mathbf{X}^{+}(t)+\mathbf{X}^{-}(t)+\mathbf{X}^{0}(t)+\mathbf{X}^{dc}(t) \tag{10}$$

$$\mathbf{X}^{+}(t)=\begin{bmatrix} x_a^{+}(t) \\ x_b^{+}(t) \\ x_c^{+}(t) \end{bmatrix}=X^{+}\begin{bmatrix} \sin\left(\omega t+\theta^{+}\right) \\ \sin\left(\omega t+\theta^{+}-2\pi/3\right) \\ \sin\left(\omega t+\theta^{+}+2\pi/3\right) \end{bmatrix} \tag{11}$$

$$\mathbf{X}^{-}(t)=\begin{bmatrix} x_a^{-}(t) \\ x_b^{-}(t) \\ x_c^{-}(t) \end{bmatrix}=X^{-}\begin{bmatrix} \sin\left(\omega t+\theta^{-}\right) \\ \sin\left(\omega t+\theta^{-}+2\pi/3\right) \\ \sin\left(\omega t+\theta^{-}-2\pi/3\right) \end{bmatrix} \tag{12}$$

$$\mathbf{X}^{0}(t)=\begin{bmatrix} x_a^{0}(t) \\ x_b^{0}(t) \\ x_c^{0}(t) \end{bmatrix}=X^{0}\begin{bmatrix} \sin\left(\omega t+\theta^{0}\right) \\ \sin\left(\omega t+\theta^{0}\right) \\ \sin\left(\omega t+\theta^{0}\right) \end{bmatrix} \tag{13}$$

$$\mathbf{X}^{dc}(t)=\begin{bmatrix} x_a^{dc}(t) \\ x_b^{dc}(t) \\ x_c^{dc}(t) \end{bmatrix}=\begin{bmatrix} X_a^{dc}e^{-\sigma_a t} \\ X_b^{dc}e^{-\sigma_b t} \\ X_c^{dc}e^{-\sigma_c t} \end{bmatrix} \tag{14}$$

The amplitude-phase information to be detected comprises X^{+}, X^{-}, X^{0}, θ^{+}, θ^{-}, and θ^{0}. Detailed detection algorithm, based on the grid transient signal given by (10), will be derived in the following. Since the mathematical derivation is cumbersome and unintuitive, Fig. 4 is framed to describe the principle and procedure of signal separation of the DDC and sequence components.

B. DDC Components Separation

Based on the time-domain expression of the grid transient signal model given by (10), all sequence components are represented by normal sinusoidal waves, whereas the DDC

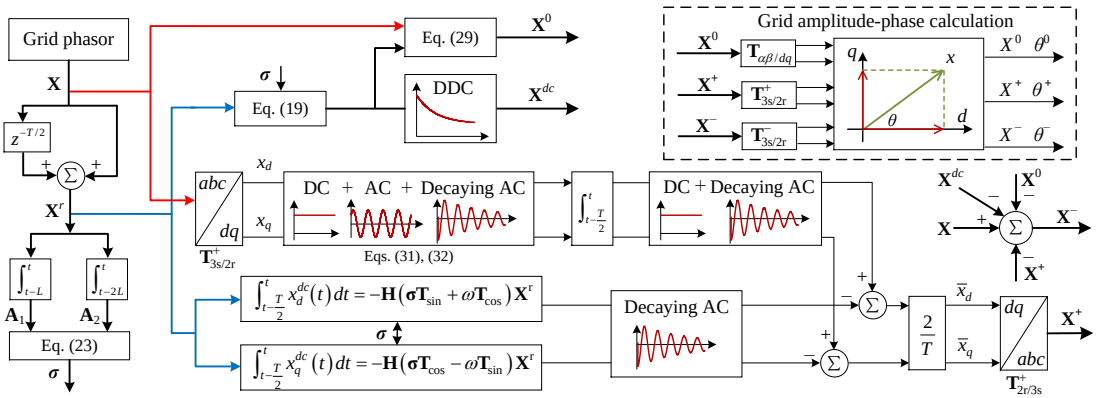

Fig. 4. Principle diagram of extraction: DDC component and sequence components.

components are intrinsically DC quantities with unchanged polarities. The latter, which are extremely important for fast amplitude-phase detection, can thus be separated by utilizing the half-wave symmetry of sinusoidal waves, i.e. (with $T = 2\pi/\omega$ being the grid period)

$$\begin{cases} \mathbf{X}^{+}(t) + \mathbf{X}^{+}(t - T/2) = 0 \\ \mathbf{X}^{-}(t) + \mathbf{X}^{-}(t - T/2) = 0 \\ \mathbf{X}^{0}(t) + \mathbf{X}^{0}(t - T/2) = 0 \end{cases} \tag{15}$$

Let us define

$$\mathbf{X}^{r}(t) = \mathbf{X}(t) + \mathbf{X}(t - T/2) \tag{16}$$

and $\mathbf{X}^{r}(t) = [x_a^r(t), x_b^r(t), x_c^r(t)]^{\mathrm{T}}$, then

$$x_k^r(t) = x_k(t) + x_k(t - T/2) \quad (k = a, b, c) \tag{17}$$

Substituting (10), (14), and (15) into (16) thoroughly eliminates the sequence components in $\mathbf{X}$, and gives

$$\mathbf{X}^{r}(t) = \mathbf{X}^{dc}(t) + \mathbf{X}^{dc}(t - T/2) = \left(\mathbf{E} + e^{\frac{T}{2}\boldsymbol{\sigma}}\right)\mathbf{X}^{dc}(t) \tag{18}$$

where $\boldsymbol{\sigma}$ and $\mathbf{E}$ are the intrinsic parameter matrix of DDC components and the 3-by-3 identity matrix, respectively, and

$$\boldsymbol{\sigma} = \begin{bmatrix} \sigma_{\mathrm{a}} & & \\ & \sigma_{\mathrm{b}} & \\ & & \sigma_{\mathrm{c}} \end{bmatrix}, \mathbf{E} = \begin{bmatrix} 1 & & \\ & 1 & \\ & & 1 \end{bmatrix}$$

Therefore, the DDC components of $\mathbf{X}$ can be obtained as

$$\mathbf{X}^{dc}(t) = \left(\mathbf{E} + e^{\frac{T}{2}\boldsymbol{\sigma}}\right)^{-1}\mathbf{X}^{r}(t) \tag{19}$$

To calculate the DDC component by (19), it is necessary to obtain the entries (decay coefficients) in the matrix $\boldsymbol{\sigma}$. To this end, definite integrals over time are performed twice for each element in $\mathbf{X}^r$. The results for phase k are given by

$$A_{k1} = \int_{t-L}^{t} x_k^r(t)\,\mathrm{d}t = \frac{X_k^{dc}}{\sigma_k}\left(1 + e^{\frac{\sigma_k T}{2}}\right)\left(e^{\sigma_k L} - 1\right)e^{-\sigma_k t} \tag{20}$$

$$A_{k2} = \int_{t-2L}^{t} x_k^r(t)\,\mathrm{d}t = \frac{X_k^{dc}}{\sigma_k}\left(1 + e^{\frac{\sigma_k T}{2}}\right)\left(e^{2\sigma_k L} - 1\right)e^{-\sigma_k t} \tag{21}$$

where L ($L > 0$) is a specified integration period.

DDC components only exist during transient. If the calculation results of (20) and (21) approach zero simultaneously, the system is in steady state, and the pertinent detection algorithm does not need to consider the influence of DDC components; otherwise, the DDC influence should be considered for accurate amplitude-phase detection.

To this end, combination of (20) and (21) gives

$$\frac{A_{k1}}{A_{k2}} = \frac{e^{\sigma_k L} - 1}{e^{2\sigma_k L} - 1} \tag{22}$$

By solving (22), the decay coefficient of DDC component in phase k is obtained as

$$\sigma_k = \frac{1}{L}\ln\left(A_{k2}/A_{k1} - 1\right) \tag{23}$$

The definite integrals (20) and (21) effectively suppress the high-frequency random noise in calculating the intrinsic parameter matrix $\boldsymbol{\sigma}$ and DDC components. The underlying principle is analogous to that of a moving average filter [22]. A larger L enables better random noise suppression, lowers random noise carried in A_{k1} and A_{k2} and, thus, results in more accurate calculation results of (19) and (23). However, its pertinent detection time will accordingly increase. A feasible solution to this contradiction will be discussed in Sec. IV.

C. Sequence Components Separation

The zero-sequence components can be extracted first by exploiting the identical elements in three phases.

1) Zero-sequence components separation: The symmetry of positive- and negative-sequence components gives

$$x_a^{+}(t) + x_b^{+}(t) + x_c^{+}(t) = 0 \tag{24}$$

$$x_a^{-}(t) + x_b^{-}(t) + x_c^{-}(t) = 0 \tag{25}$$

The sum of zero-sequence components is

$$x_a^{0}(t) + x_b^{0}(t) + x_c^{0}(t) = 3X^{0}\sin\left(\omega t + \theta^{0}\right) \tag{26}$$

The three-phase sum of DDC components can be obtained by considering the elements of $\mathbf{X}^{dc}$ [see (19)], namely:

$$x_a^{dc}(t) + x_b^{dc}(t) + x_c^{dc}(t) = \sum_{k=a,b,c} x_k^{dc}(t) \tag{27}$$

By considering that

$$x_k(t) = x_k^+(t) + x_k^-(t) + x_k^0(t) + x_k^{dc}(t) \quad (k = a, b, c) \tag{28}$$

and by respectively adding the left- and right-hand sides of (24), (25), (26), and (27), the zero-sequence components can be obtained as

$$X^0 \sin\left(\omega t + \theta^0\right) = \frac{1}{3} \sum_{k=a,b,c} \left[x_k(t) - x_k^{dc}(t)\right] \tag{29}$$

2) Positive-sequence components separation: From the physical meaning of Park's Transformation, specific sequence components can be converted into DC signals in the pertinent *dq*-frame, whereas the residual sequence and DDC components will be converted into AC waves of different types. Accordingly, various signal components can be separated.

The positive-sequence Park's Transformation writes

$$\mathbf{X}_{dq}(t) = \mathbf{T}_{3s/2r}^{+} \mathbf{X}(t) \tag{30}$$

where $\mathbf{X}_{dq}(t) = \begin{bmatrix} x_d(t) & x_q(t) \end{bmatrix}^{\mathrm{T}}$

$$\mathbf{T}_{3s/2r}^{+} = \frac{2}{3} \begin{bmatrix} \sin\omega t & \sin(\omega t - 2\pi/3) & \sin(\omega t + 2\pi/3) \\ \cos\omega t & \cos(\omega t - 2\pi/3) & \cos(\omega t + 2\pi/3) \end{bmatrix}$$

Hence, $\mathbf{X}$ in positive-sequence *dq*-frame is described as

$$x_d(t) = X^+ \cos\theta^+ - X^- \cos\left(2\omega t + \theta^-\right) + x_d^{dc}(t) \tag{31}$$

$$x_q(t) = X^+ \sin\theta^+ + X^- \sin\left(2\omega t + \theta^-\right) + x_q^{dc}(t) \tag{32}$$

where

$$\begin{aligned} x_d^{dc}(t) = & \frac{2}{3}\left[X_a^{dc} e^{-\sigma_a t} \sin\omega t + X_b^{dc} e^{-\sigma_b t} \sin(\omega t - 2\pi/3)\right. \\ & \left. + X_c^{dc} e^{-\sigma_c t} \sin(\omega t + 2\pi/3)\right] \end{aligned} \tag{33}$$

$$\begin{aligned} x_q^{dc}(t) = & \frac{2}{3}\left[X_a^{dc} e^{-\sigma_a t} \cos\omega t + X_b^{dc} e^{-\sigma_b t} \cos(\omega t - 2\pi/3)\right. \\ & \left. + X_c^{dc} e^{-\sigma_c t} \cos(\omega t + 2\pi/3)\right] \end{aligned} \tag{34}$$

It is noted that $\mathbf{X}$ in positive-sequence *dq*-frame encompasses three types of components, i.e., 1) DC components pertinent to positive-sequence components in *abc*-frame, 2) second-order harmonics pertinent to negative-sequence components in *abc*-frame, and 3) decaying AC waves pertinent to DDC components in *abc*-frame. Among them, the second harmonics in *dq*-frame can be eliminated by exploiting the full-wave symmetry of sinusoidal signals [22], i.e.,

$$\int_{t-\frac{T}{2}}^{t} X^- \sin\left(2\omega t + \theta^-\right) dt \equiv \int_{t-\frac{T}{2}}^{t} X^- \cos\left(2\omega t + \theta^-\right) dt \equiv 0 \tag{35}$$

Accordingly, the decaying AC waves in positive-sequence *dq*-frame can be calculated by

$$\begin{aligned} \int_{t-\frac{T}{2}}^{t} x_d^{dc}(t)\, dt = & \frac{2}{3}\left[\int_{t-\frac{T}{2}}^{t} X_a^{dc} e^{-\sigma_a t} \sin\omega t dt\right. \\ & + \int_{t-\frac{T}{2}}^{t} X_b^{dc} e^{-\sigma_b t} \sin(\omega t - 2\pi/3)\, dt \\ & \left. + \int_{t-\frac{T}{2}}^{t} X_c^{dc} e^{-\sigma_c t} \sin(\omega t + 2\pi/3)\, dt\right] \\ = & -\mathbf{H}\left(\boldsymbol{\sigma}\mathbf{T}_{\sin} + \omega\mathbf{T}_{\cos}\right)\mathbf{X}^r \end{aligned} \tag{36}$$

$$\begin{aligned} \int_{t-\frac{T}{2}}^{t} x_q^{dc}(t)\, dt = & \frac{2}{3}\left[\int_{t-\frac{T}{2}}^{t} X_a^{dc} e^{-\sigma_a t} \cos\omega t dt\right. \\ & + \int_{t-\frac{T}{2}}^{t} X_b^{dc} e^{-\sigma_b t} \cos(\omega t - 2\pi/3)\, dt \\ & \left. + \int_{t-\frac{T}{2}}^{t} X_c^{dc} e^{-\sigma_c t} \cos(\omega t + 2\pi/3)\, dt\right] \\ = & -\mathbf{H}\left(\boldsymbol{\sigma}\mathbf{T}_{\cos} - \omega\mathbf{T}_{\sin}\right)\mathbf{X}^r \end{aligned} \tag{37}$$

where $\mathbf{H} = \frac{2}{3}\begin{bmatrix} \frac{1}{\omega^2+\sigma_a^2} & \frac{1}{\omega^2+\sigma_b^2} & \frac{1}{\omega^2+\sigma_c^2} \end{bmatrix}$

$$\mathbf{T}_{\sin} = \begin{bmatrix} \sin(\omega t) & & \\ & \sin(\omega t - 2\pi/3) & \\ & & \sin(\omega t + 2\pi/3) \end{bmatrix}$$

$$\mathbf{T}_{\cos} = \begin{bmatrix} \cos(\omega t) & & \\ & \cos(\omega t - 2\pi/3) & \\ & & \cos(\omega t + 2\pi/3) \end{bmatrix}$$

By integrating (31) and (32) over half grid period and considering (35), (36), and (37), the positive-sequence components in positive-sequence *dq*-frame [i.e., the steady-state DC components in (31) and (32)] can be obtained, yielding

$$\begin{cases} \bar{x}_d(t) = X^+ \cos\theta^+ = \dfrac{2}{T}\left[\displaystyle\int_{t-\frac{T}{2}}^{t} x_d(t)\, dt - \int_{t-\frac{T}{2}}^{t} x_d^{dc}(t)\, dt\right] \\ \qquad\qquad = \dfrac{2}{T}\left[\displaystyle\int_{t-\frac{T}{2}}^{t} x_d(t)\, dt + \mathbf{H}\left(\sigma\mathbf{T}_{\sin} + \omega\mathbf{T}_{\cos}\right)\mathbf{X}^r\right] \\ \bar{x}_q(t) = X^+ \sin\theta^+ = \dfrac{2}{T}\left[\displaystyle\int_{t-\frac{T}{2}}^{t} x_q(t)\, dt - \int_{t-\frac{T}{2}}^{t} x_q^{dc}(t)\, dt\right] \\ \qquad\qquad = \dfrac{2}{T}\left[\displaystyle\int_{t-\frac{T}{2}}^{t} x_q(t)\, dt + \mathbf{H}\left(\sigma\mathbf{T}_{\cos} - \omega\mathbf{T}_{\sin}\right)\mathbf{X}^r\right] \end{cases} \tag{38}$$

Hence, the positive-sequence components of $\mathbf{X}$ can be obtained as

$$\begin{aligned} \mathbf{X}^+ &= \mathbf{T}_{2r/3s}^{+} \begin{bmatrix} \bar{x}_d(t) \\ \bar{x}_q(t) \end{bmatrix} \\ &= \frac{2}{T}\mathbf{T}_{2r/3s}^{+}\left(\int_{t-\frac{T}{2}}^{t} \mathbf{X}_{dq} dt + \begin{bmatrix} \mathbf{H}\left(\boldsymbol{\sigma}\mathbf{T}_{\sin} + \omega\mathbf{T}_{\cos}\right)\mathbf{X}^r \\ \mathbf{H}\left(\boldsymbol{\sigma}\mathbf{T}_{\cos} - \omega\mathbf{T}_{\sin}\right)\mathbf{X}^r \end{bmatrix}\right) \end{aligned} \tag{39}$$

where

$$\mathbf{T}_{2r/3s}^{+} = \begin{bmatrix} \sin\omega t & \cos\omega t \\ \sin(\omega t - 2\pi/3) & \cos(\omega t - 2\pi/3) \\ \sin(\omega t + 2\pi/3) & \cos(\omega t + 2\pi/3) \end{bmatrix}$$

3) Negative-sequence components separation: By substituting (19), (29), and (39) into (10), the negative-sequence components of $\mathbf{X}$ can be obtained as

$$\mathbf{X}^-(t) = \mathbf{X}(t) - \mathbf{X}^+(t) - \mathbf{X}^0(t) - \mathbf{X}^{dc}(t) \tag{40}$$

D. Grid Amplitude-Phase Calculation

1) Positive-sequence information: The amplitude and phase of $\mathbf{X}^+$ can be obtained by (38) as

$$\begin{cases} X^+ = \sqrt{\left[\bar{x}_d\left(t\right)\right]^2 + \left[\bar{x}_q\left(t\right)\right]^2} \\ \theta^+ = \arctan\left[\dfrac{\bar{x}_q\left(t\right)}{\bar{x}_d\left(t\right)}\right] \end{cases} \tag{41}$$

Accurate results of $\bar{x}_d$ and $\bar{x}_q$ can be obtained after half period of integration [see (38)]. Accordingly, the precise amplitude and phase extraction of $\mathbf{X}^+$ takes 0.5 grid cycle, which is 10 ms for a 50 Hz-power grid.

2) Negative-sequence information: The negative-sequence component $\mathbf{X}^-$, based on the pertinent relation of three phases, can be converted into DC quantities via the negative-sequence Park's Transformation, yielding

$$\mathbf{X}_{dq}^-\left(t\right) = \mathbf{T}_{3s/2r}^-\mathbf{X}^-\left(t\right) \tag{42}$$

where $\mathbf{X}_{dq}^-\left(t\right) = \begin{bmatrix} x_d^-\left(t\right) & x_q^-\left(t\right) \end{bmatrix}^{\mathrm{T}}$

$$\mathbf{T}_{3s/2r}^- = \frac{2}{3}\begin{bmatrix} \sin\omega t & \sin\left(\omega t + 2\pi/3\right) & \sin\left(\omega t - 2\pi/3\right) \\ \cos\omega t & \cos\left(\omega t + 2\pi/3\right) & \cos\left(\omega t - 2\pi/3\right) \end{bmatrix}$$

By substituting (40) into (42), $\mathbf{X}^-$ in negative-sequence *dq*-frame can be reformulated as

$$\begin{cases} x_d^-\left(t\right) = X^-\cos\theta^- \\ x_q^-\left(t\right) = X^-\sin\theta^- \end{cases} \tag{43}$$

Analogously, the amplitude and phase of $\mathbf{X}^-$ can be obtained by (43) as

$$\begin{cases} X^- = \sqrt{\left[x_d^-\left(t\right)\right]^2 + \left[x_q^-\left(t\right)\right]^2} \\ \theta^- = \arctan\left[\dfrac{x_q^-\left(t\right)}{x_d^-\left(t\right)}\right] \end{cases} \tag{44}$$

According to (44), the time required to extract the amplitude and phase information of $\mathbf{X}^-$ is fully determined by x_d^- and x_q^-, which are obtained through (40) and (42). Among them, (42) involves pure algebraic operation that takes a negligible time. Obtaining the DDC and zero-sequence components in (40) both require a delay of half grid cycle, meanwhile the same time of integration is needed for acquiring $\mathbf{X}^+$ in (40). Since these three components are being extracted simultaneously, the accurate amplitude and phase extraction of $\mathbf{X}^-$ consumes an overall time of half grid cycle.

3) Zero-sequence information: Different from other sequence components, the zero-sequence component is characterized by a common phase, hence Park's Transformation cannot be directly performed. An orthogonal signal generation (OSG) algorithm is generally necessary for constructing a virtual signal orthogonal to the zero-sequence component, with the aim of performing transformation from $\alpha\beta$- to *dq*-frame described by

$$\begin{bmatrix} x_d^0\left(t\right) \\ x_q^0\left(t\right) \end{bmatrix} = \mathbf{T}_{\alpha\beta/dq}\begin{bmatrix} x_\alpha\left(t\right) \\ x_\beta\left(t\right) \end{bmatrix} \tag{45}$$

where

$$\mathbf{T}_{\alpha\beta/dq} = \begin{bmatrix} \sin\omega t & \cos\omega t \\ \cos\omega t & -\sin\omega t \end{bmatrix}$$

In this manuscript, the zero-sequence component obtained by (29) is used as the α-axis signal in (45), and the β-axis signal is obtained via an OSG algorithm [23] with fast response (within 2 ms). Then

$$x_\beta\left(t\right) = X^0\cos\left(\omega t + \theta^0\right) \tag{46}$$

Substituting the α- and β-axis signals into (45) gives

$$\begin{cases} x_d^0\left(t\right) = X^0\cos\theta^0 \\ x_q^0\left(t\right) = X^0\sin\theta^0 \end{cases} \tag{47}$$

Similarly, the amplitude and phase of the zero-sequence components can be obtained as

$$\begin{cases} X^0 = \sqrt{\left[x_d^0\left(t\right)\right]^2 + \left[x_q^0\left(t\right)\right]^2} \\ \theta^0 = \arctan\left[\dfrac{x_q^0\left(t\right)}{x_d^0\left(t\right)}\right] \end{cases} \tag{48}$$

Calculation of (48) requires x_d^0 and x_q^0 signals obtained from (45). Calculation of the α-axis input signal in (45) requires the use of (29) and a delay of 0.5 grid cycle. Meanwhile, 2 ms is consumed by the OSG algorithm in order to obtain the β-axis signal in (45) from the α-axis signal. Since the calculation of β-axis signal lags behind that of α-axis signal, the overall time to accurately obtain the amplitude and phase information of the zero-sequence components is about 12 ms.

IV. Performance Enhancement Solution

To enhance the detection performance in terms of response speed, anti-noise ability and reliability, several solutions are proposed in this manuscript, encompassing a multi-component parallel-detection structure, iterative variable-interval integration algorithm, and multi-DDC synthesis technology. These solutions can also reduce the complexity and computational burden, enabling the detection algorithm to be directly integrated into the existing embedded processor of converters.

A. Multi-Component Parallel-Detection Structure

Since transient conditions have additional DDC components compared to steady-state ones, by inserting the proposed DDC detection algorithm prior to the typical sequence component extraction block, the asymmetric signal without DDC can be obtained [see Fig. 5(a)]. Based on the signal flow, the DDC detection block and the sequence component detection block form a series structure. Since the DDC detection requires about 0.5 grid cycle, and so does the typical sequence component extraction algorithm (based on the interference filtering method in *dq*-frame), the total detection time of the series structure in Fig. 5(a) takes about 1 grid cycle.

To significantly reduce the detection time, the DDC component and sequence components must be extracted simultaneously, which can be achieved by the proposed multi-component parallel-detection structure [see Fig. 5(b)]. In this structure, the respective information of different component detection blocks is used interactively to eliminate the interference of other components to the target component detection. As previously mentioned, since the detection time of each

TABLE I
COMPARISON OF DDC DETECTION TECHNIQUES.

Algorithm	Response time	Stable precision	Computation load	Applicable scenario
Empirical mode decomposition (EMD)	2.25 cycles	High	High	Fault location and relay applications
Intrinsic time-scale decomposition (ITD)	1 cycle	High	High	Digital distance-relaying application
Volterrra least mean square/fourth filter	1 cycle	Medium	High	PQ monitoring and relay applications
Series detection structure in dq frame	1 cycle	High	Low	Embedded controller of power converters
Improved discrete Fourier transform (DFT)	0.75 cycles	Medium	Low	Embedded controller of power converters
Mathematical morphology method	0.5 cycle	Low	High	Calibration and coordination of protection devices
Proposed method	0.5 cycle	High	Low	Embedded controller of power converters

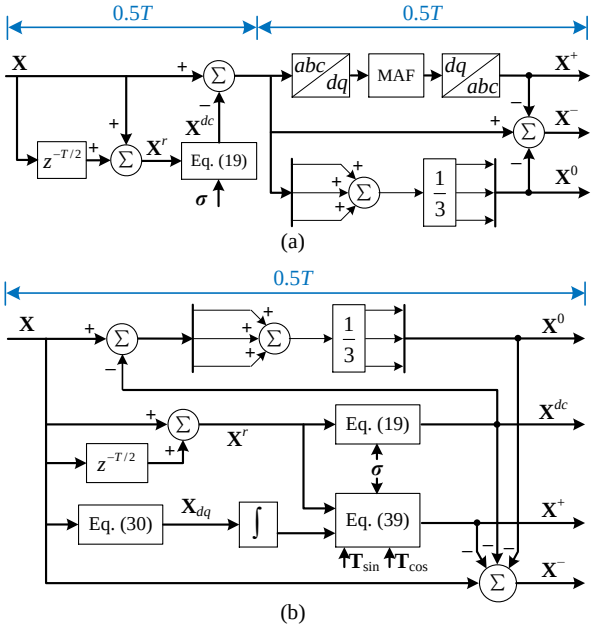

Fig. 5. Schematic diagrams of grid amplitude-phase detection methods based on (a) series and (b) parallel structures, respectively.

component is 0.5 grid cycle, the overall detection time of the parallel scheme is about 0.5 grid cycle as well. Hence, the critical indicator of detection algorithm, namely, response speed, has been essentially improved, as shown in Table I.

B. Iterative Variable-Interval Integral

1) Fixed-interval algorithm: The proposed algorithm uses multiple integral operations. Their direct implementation by cumulative summation is associated with a large amount of addition operations, especially with long integral intervals. To reduce the computational burden of embedded processor, an iterative integral algorithm in discrete-time domain with fixed interval is first proposed in this manuscript.

By denoting the sample time of the digital control system as T_s, the number of samples M in 0.5 grid cycle, and the number of samples N in the integral period L [see (20) and (21)] yield

$$\begin{cases} M = \text{round}\left(0.5T/T_s\right) \\ N = \text{round}\left(L/T_s\right) \end{cases} \tag{49}$$

Hence, at the n-th sampling point, the discrete-time expressions of (20) and (21) are given by

$$A_{k1}\left(n,N\right) = T_s \sum_{i=n-N+1}^{n} x_k^r\left(i\right) \tag{50}$$

$$A_{k2}\left(n,N\right) = T_s \sum_{i=n-2N+1}^{n} x_k^r\left(i\right) \tag{51}$$

As previously discussed, with reference to the disturbance time ($t = 0$), calculation results of (20) and (21) can accurately trace their actual values after the response time of nearly half grid cycle (corresponding to M samples). Specifically, in the discrete-time domain, for accurate output results of (50) and (51), the pertinent sampling time n must satisfy

$$n \geq M + N + 1 \tag{52}$$

$$n \geq M + 2N + 1 \tag{53}$$

At the $(n-1)$-th sampling, the discrete expressions of (20) and (21) are

$$A_{k1}\left(n-1,N\right) = T_s \sum_{i=n-N}^{n-1} x_k^r\left(i\right) \tag{54}$$

$$A_{k2}\left(n-1,N\right) = T_s \sum_{i=n-2N}^{n-1} x_k^r\left(i\right) \tag{55}$$

By combining (50) and (54), we have

$$\begin{aligned} A_{k1}\left(n,N\right) =& A_{k1}\left(n-1,N\right) \\ &+ T_s\left[x_k^r\left(n\right) - x_k^r\left(n-N\right)\right] \end{aligned} \tag{56}$$

Analogously, the combination of (51) and (55) gives

$$\begin{aligned} A_{k2}\left(n,N\right) =& A_{k2}\left(n-1,N\right) \\ &+ T_s\left[x_k^r\left(n\right) - x_k^r\left(n-2N\right)\right] \end{aligned} \tag{57}$$

(56) and (57) gives the discrete-time iterative integrals with fixed intervals. Use of (50) and (51) for discrete-time integrals requires $(3N-2)$ addition operations, yet use of the iterative algorithm given by (56) and (57) requires merely 4 addition operations. This significantly reduces the computational burden of the embedded processor especially when a large N value is adopted for better noise suppression.

2) Variable-interval algorithm: As previously discussed, random noise suppression and detection time should be considered comprehensively when calculating the intrinsic parameter matrix $\boldsymbol{\sigma}$ and DDC components. This holds also for the discrete-time iterative algorithm given by (56) and (57). Large L or N value indicates more sampled data, which facilitate the suppression of high-frequency random noise and the improvement of calculation accuracy, yet also increase the pertinent detection time.

To fully exploit the above algorithm, and achieve fast response and improved immunity against noise, an iterative variable-interval integral algorithm is developed. At the beginning of algorithm, a small value of N is set ($N = N_{\text{lower}}$) such that the DDC value outputs shortly after half grid period. Then, the value of N successively (namely, the integral interval) increases with the update of sampling data, until an upper limit N_{upper} is reached.

Assuming the integral interval to be $(N-1)$ at the $(n-1)$-th sampling, the discrete integrals given by (54) and (55) are adapted as

$$A_{k1}\left(n-1, N-1\right) = T_s \sum_{i=n-N+1}^{n-1} x_k^r\left(i\right) \tag{58}$$

$$A_{k2}\left(n-1, N-1\right) = T_s \sum_{i=n-2N+2}^{n-1} x_k^r\left(i\right) \tag{59}$$

By combining (50) and (58), we have

$$A_{k1}\left(n, N\right) = A_{k1}\left(n-1, N-1\right) + T_s x_k^r\left(n\right) \tag{60}$$

Analogously, the combination of (51) and (59) gives

$$\begin{aligned} A_{k2}\left(n, N\right) =& A_{k2}\left(n-1, N-1\right) \\ &+ T_s\left[x_k^r\left(n\right) + x_k^r\left(n-2N+1\right)\right] \end{aligned} \tag{61}$$

It is worth mentioning that the relationship between the sampling time n and the integral interval N must satisfy (52) and (53) simultaneously. When the integral interval reduces to $(N-1)$, (52) and (53) can be rewritten as

$$n \geq M + N \tag{62}$$

$$n \geq M + 2N - 1 \tag{63}$$

When the integral interval increases from $N-1$ to N, from (52) and (62), the sampling number n also increases by 1; however, comparison between (53) and (63) indicates that n needs to be increased by 2. Since increasing the integral interval N requires the satisfaction of these conditions simultaneously, the update rate of the sampling data must be at least twice that of the integral interval N.

To this end, the previous integrals (20) and (21) can be updated as shown by procedure $A_k(n, N)$ in Algorithm 1. Specifically,

- For $N < N_{\text{upper}}$, an iterative variable-interval integral algorithm is used. When n is odd, (56) and (57) are adopted, and the integral interval N remains unchanged; when n is even, (60) and (61) are exploited, and the integral interval is incremented by 1.
- For large enough N ($N = N_{\text{upper}}$) to notably suppress the high-frequency random noise, the iterative fixed-interval algorithm given by (56) and (57) are used to calculate (20) and (21). The integral interval maintains its upper limit value N_{upper}.

Algorithm 1

Require: $n \geq M + 2N_{\text{lower}} - 1$

procedure $A_k(n, N)$
  if $n = M + 2N_{\text{lower}} - 1$ **then**
    calculate $A_{k1}(n, N)$ by Eq. (50)
    calculate $A_{k2}(n, N)$ by Eq. (51)
  else
    if $\text{mod}(N, 2) = 0$ & $N <= N_{\text{upper}}$ **then**
      $N \leftarrow N + 1$
      calculate $A_{k1}(n, N)$ by Eq. (60)
      calculate $A_{k2}(n, N)$ by Eq. (61)
    else
      calculate $A_{k1}(n, N)$ by Eq. (56)
      calculate $A_{k2}(n, N)$ by Eq. (57)
    end if
  end if
  $n \leftarrow n + 1$
end procedure

By adopting the variable integral interval, the accuracy of the calculation result will be gradually improved. Accordingly, this algorithm can effectively suppress the high-frequency random noise without lowering the response speed of detection, meanwhile restricting the computational burden of the embedded processor.

C. Multi-Mode DDC Components Synthesis

In the event of an asymmetric disturbance, transient electrical quantities can exhibit multiple modes of DDC components with different decaying coefficients. If the algorithm is directly derived based on the mathematical expression containing multiple DDC components, the algorithm complexity will sharply increase. In this manuscript, (7) is used to synthesize the multi-mode DDC components into an equivalent one, thereby simplifying the algorithm. Mathematical induction is used to prove the validity of (7).

Proof. (7) holds for any positive integer number n.

- *Base case:* Show that (7) holds for n taking the smallest positive integer number 1.
  It is clearly true: $P(1) = A_1 e^{-\sigma_1 t} = A_1^{\sum} e^{-\sigma_1^{\sum} t}$ holds for $A_1^{\sum} = A_1$, $\sigma_1^{\sum} = \sigma_1$.
- *Inductive step:* Show that for any $k \geq 1$, if (7) holds for $P(k)$, then (7) also holds for $P(k+1)$.
  Assume the induction hypothesis that for a particular k, the single case $n = k$ holds, meaning that

$$\sum_{i=1}^{k} A_i e^{-\sigma_i t} = A_k^{\sum} e^{-\sigma_k^{\sum} t} \tag{64}$$

  As shown in Fig. 6, any two DDC components must intersect at a certain time t_{I}, either be the transient starting

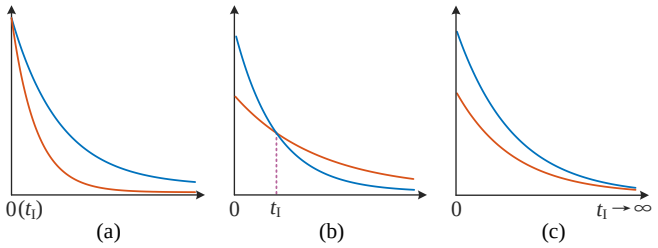

Fig. 6. Two DDC components intersecting at transient (a) starting time, (b) middle time, and (c) final time, respectively.

time ($t_1 = 0$), the final time ($t_1 \to \infty$), or an instant during the decaying process. Hence, when $n = k + 1$,

$$\begin{aligned}\sum_{i=1}^{k+1} A_i e^{-\sigma_i t} &= \sum_{i=1}^{k} A_i e^{-\sigma_i t} + A_{k+1} e^{-\sigma_{k+1} t} \\ &= A_k^{\sum} e^{-\sigma_k^{\sum} t} + A_{k+1} e^{-\sigma_{k+1} t} \\ &= A_{k+1}^{\sum} e^{-\sigma_{k+1}^{\sum} t}\end{aligned} \tag{65}$$

In order to obtain the expression of $A_{k+1}^{\sum}$, let $t = 0$, then

$$A_{k+1}^{\sum} = A_k^{\sum} + A_{k+1} \tag{66}$$

Similarly, to obtain the expression of $\sigma_{k+1}^{\sum}$, let $t = t_1$, then

$$A_k^{\sum} e^{-\sigma_k^{\sum} t_1} = A_{k+1} e^{-\sigma_{k+1} t_1} = \frac{1}{2} A_{k+1}^{\sum} e^{-\sigma_{k+1}^{\sum} t_1} \tag{67}$$

Therefore,

$$t_1 = \frac{\ln A_k^{\sum} - \ln A_{k+1}}{\sigma_k^{\sum} - \sigma_{k+1}} \tag{68}$$

It is obvious that when $A_k^{\sum} = A_{k+1}$, the DDC components intersect at $t_1 = 0$; when $\sigma_k^{\sum} = \sigma_{k+1}$, the components intersect at the final time ($t_1 \to \infty$).
By substituting (68) into (67), we have

$$\sigma_{k+1}^{\sum} = \sigma_{k+1} - \frac{\ln 2A_{k+1} - \ln A_{k+1}^{\sum}}{\ln A_k^{\sum} - \ln A_{k+1}} \left(\sigma_k^{\sum} - \sigma_{k+1}\right) \tag{69}$$

By combining (65), (66), and (69), it is clear that (7) still holds when $n = k + 1$.

- *Conclusion*: (7) holds for any positive integer n. ■

In summary, according to the principle of mathematical induction, synthesizing multi-mode DDC components into one DDC component is fully reasonable.

V. Verification

In this work, effectiveness and superiority of the proposed amplitude-phase detection algorithm are verified on the hardware-in-the-loop (HIL) experiment platform (see Fig. 7), which emulates the DDC components involved voltage/current signals by using a set of real-time simulation platform and realizes the presented algorithm by using a DSP-based controller board for grid-tied converter. The generated test signal (see Fig. 8) according to (10) is three-phase symmetric with only positive-sequence component before the disturbance, and its amplitude and phase are 0.25 p.u. and $-\pi/2$, respectively. The three-phase parameters after the disturbance are shown in Table II. The DDC component during transient is determined by (6). On this basis, comparative experiments on amplitude-phase detection are conducted when ignoring and considering the influence of DDC components. Besides, an extreme case with maximum frequency fluctuation is considered after the disturbance. The sample frequency of the embedded control system is maintained at 10 kHz.

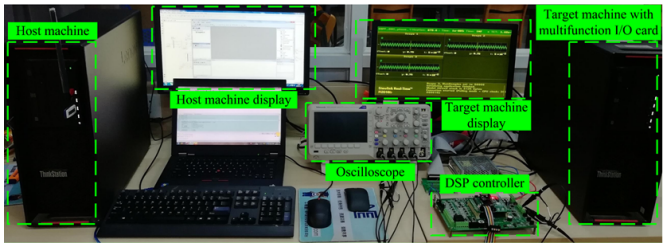

Fig. 7. Hardware setup of the experimental platform adopted in this work.

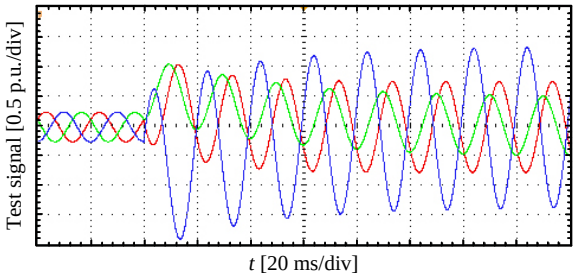

Fig. 8. Three-phase transient electrical signal for testing.

TABLE II
Main Parameters of Testing Signal

Parameter	Value	Parameter	Value	Parameter	Value
X^+	0.75 p.u.	θ^+	$\pi/4$	L^+/R^+	0.04 s
X^-	0.50 p.u.	θ^-	$\pi/12$	L^-/R^-	0.02 s
X^0	0.25 p.u.	θ^0	$-\pi/6$	L^0/R^0	0.03 s

The comparative results are shown in Figs. 9-12. In the absence of DDC component suppression measures, due to the large X/R ratio of the high-voltage power system, the DDC component during transient inevitably appears in the detected sequence component waveforms, causing severe asymmetry of sequence components (see Fig. 9) that lasts for nearly 5 grid cycles. The extracted amplitude and phase are also affected by severe oscillations with decaying amplitude (see green curves in Fig. 10). These results, if applied to converter control and protection, will lower the converter performance in terms of disturbance suppression and fault ride-through.

When the proposed scheme is adopted, the detection results of sequence components (see Fig. 11) and amplitude-phase information (see red curves in Fig. 10) from the three-phase transient signal quickly track the actual values after approximately 0.5 grid cycle. By effectively suppressing the DDC influence, the asymmetry of extracted sequence components is avoided, and transient amplitudes of sequence components are

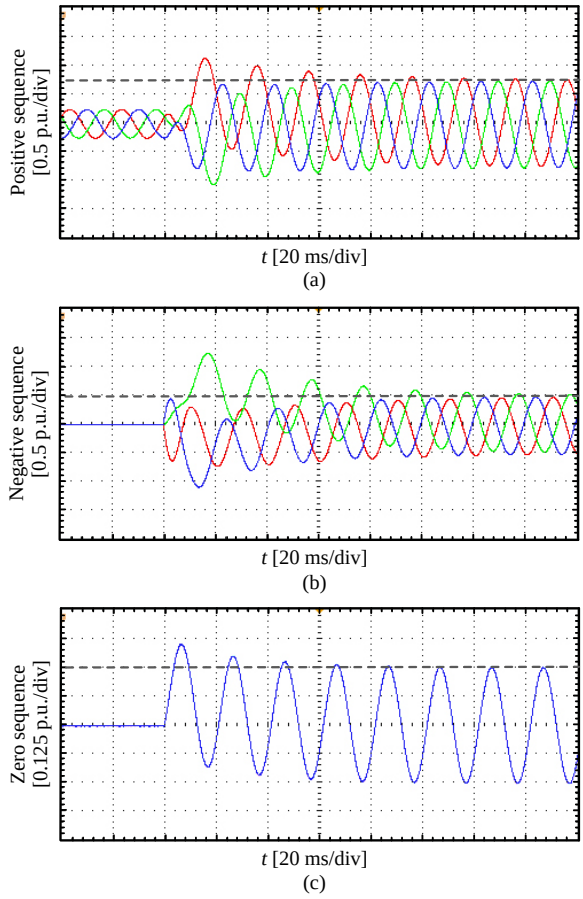

Fig. 9. Detected sequence components without considering DDC component.

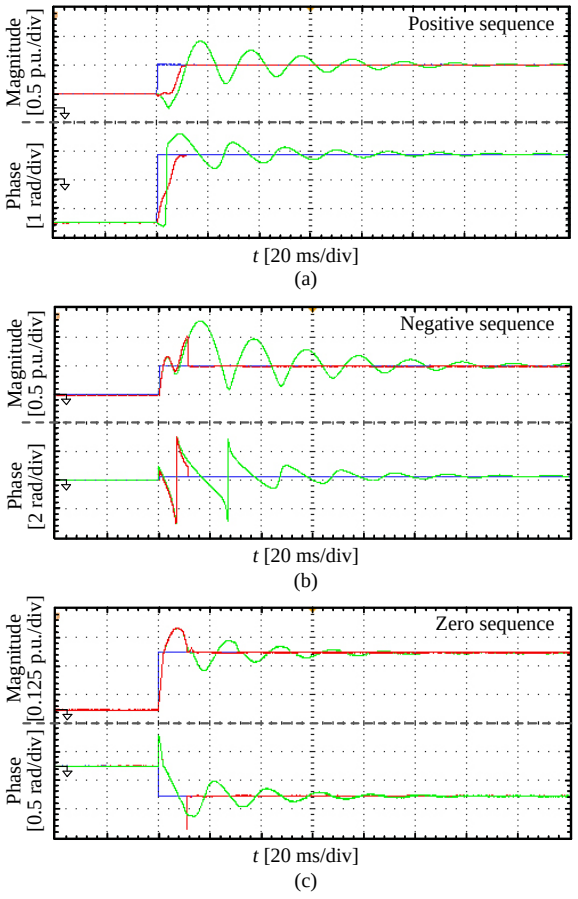

Fig. 10. Detected amplitudes and phases with (red curves)/without (green curves) consideration of the DDC influence. Blue curves are reference signals.

notably reduced as well. The extracted amplitude and phase are also free from obvious oscillations, providing accurate and reliable grid amplitude-phase information for subsequent converter control and protection.

Achieving zero steady-state error is one operating objective of the converter system under steady-state conditions, yet it is not applicable for a system under transient conditions. Indeed, in the transient process caused by large disturbances, the major focus of converter detection, control and protection are to quickly and effectively suppress the transient impact caused by drastic changes in the grid power flow, ensuring the safety and stability of converters and power grids. Besides, the frequency deviation range of high-voltage power systems allowed by the grid code is typically less than 1 Hz (and 0.2 Hz for the steady-state condition), otherwise the grid protection device will be triggered. Based on the these facts, the proposed algorithm considers the grid frequency to be constant in order to effectively simplify the calculation and shorten the detection time. When the system resumes the steady-state operation, the detection algorithm can be switched to the conventional PLL algorithm according to the zero-error requirement on steady-state performance.

To this end, validity of the proposed scheme is also verified when considering the extreme case of frequency change, namely, the frequency suddenly drops by 1 Hz at the disturbance instant, and the pertinent results are shown in Fig. 12. The detection error is significant when neglecting the DDC component (see green curves in Fig. 12). However, by considering the DDC component during the detection, and simply neglecting the frequency change, the detected results (see red curves in Fig. 12) are greatly improved. Hence, in the presence of grid frequency change within the allowable range defined by the grid code, the accuracy and rapidity of the proposed scheme can still meet the requirements of converter control and protection.

VI. Conclusion

In application scenarios of medium- and high-voltage power grids with large X/R ratios, major disturbances such as faults and heavy load switching result in large-amplitude and long-duration DDC components in transient electrical quantities of the power grid. These components greatly affect the functions of various links. In such a case, the transient process of power flow can no longer be viewed as instantaneous.

In this work, the amplitude-phase detection scheme based on a multi-component parallel-detection structure is proposed. The scheme accurately extracts the DDC and sequence components within approximately 0.5 grid cycle, and provides the amplitude and phase information of each sequence component. The proposed iterative variable-interval integral algorithm in discrete-time domain effectively improves the anti-noise abil-

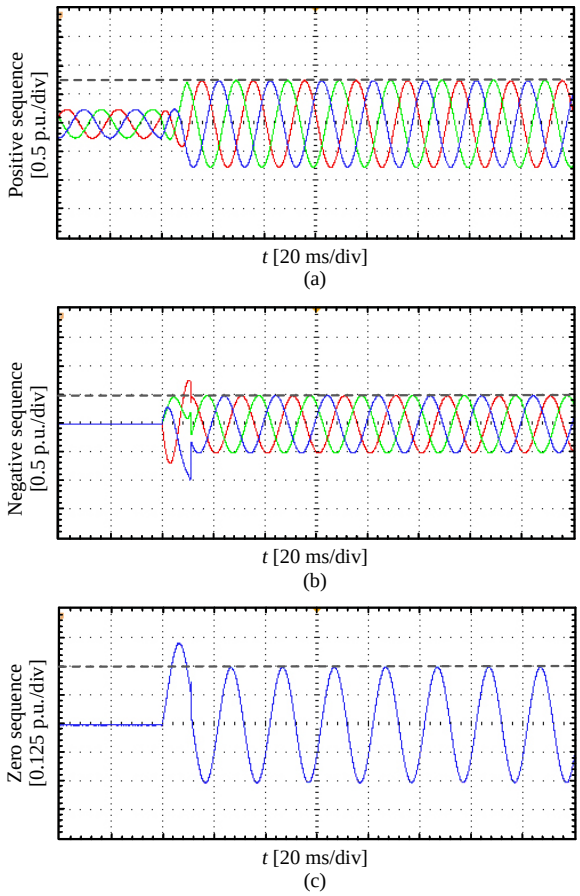

Fig. 11. Detected sequence components with considering DDC component

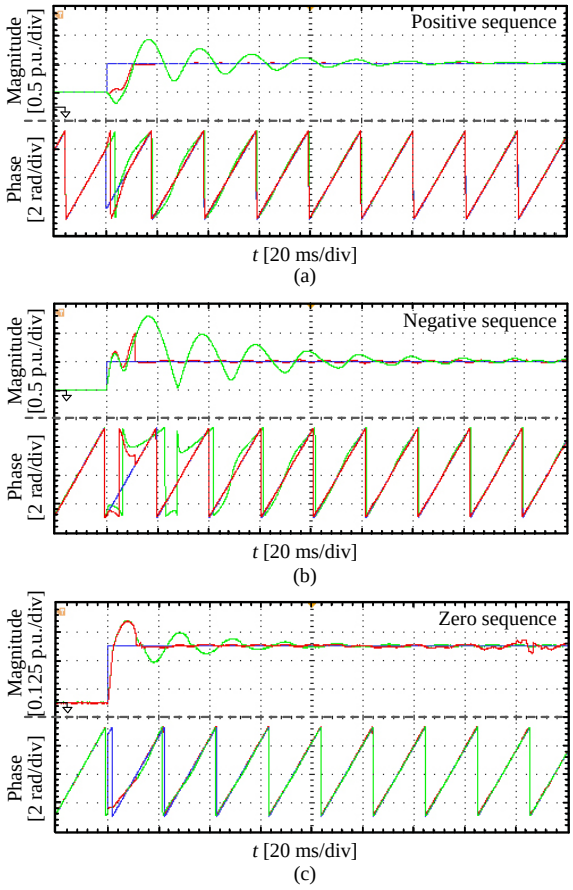

Fig. 12. In the event of sudden frequency change, detected amplitudes and phases with (red curves)/without (green curves) consideration of the DDC influence. Blue curves are reference signals. Real-time phases (after taking the remainder with 2π) are displayed.

ity and reduces the calculation amount. As a result, this algorithm can be directly integrated into the embedded processor of converters. The feasibility and advancement of the proposed algorithm are verified by experiment results.

REFERENCES

[1] K. W. Min and S. Santoso, "DC offset removal algorithm for improving location estimates of momentary faults," *IEEE Trans. Smart Grid*, vol. 9, no. 6, pp. 5503–5511, 2018.

[2] L. Xiong, X. Liu, C. Zhao, and F. Zhuo, "A fast and robust real-time detection algorithm of decaying dc transient and harmonic components in three-phase systems," *IEEE Trans. Power Electron.*, vol. 35, no. 4, pp. 3332–3336, 2020.

[3] Y. He, M. Wang, and Z. Xu, "Coordinative low-voltage-ride-through control for the wind-photovoltaic hybrid generation system," *IEEE J. Emerg. Sel. Topics Power Electron.*, vol. 8, no. 2, pp. 1503–1514, 2020.

[4] M. S. Reza and M. M. Hossain, "A demodulation-based method for instantaneous phase angle estimation of unbalanced three-phase voltage systems," *IEEE J. Emerg. Sel. Topics Power Electron.*, to be published, doi: 10.1109/JESTPE.2021.3065231.

[5] M. S. Reza, F. Sadeque, M. M. Hossain *et al.*, "Three-phase PLL for grid-connected power converters under both amplitude and phase unbalanced conditions," *IEEE Trans. Ind. Electron.*, vol. 66, no. 11, pp. 8881–8891, 2019.

[6] C. J. Nwobu, A. M. Nakiganda, and L. Zhang, "Grid voltage synchronization for unbalanced voltages using the energy operator," *IEEE J. Emerg. Sel. Topics Power Electron.*, vol. 5, no. 3, pp. 1415–1424, 2017.

[7] P. Piya, M. Ebrahimi, M. Karimi-Ghartemani, and S. A. Khajehoddin, "Fault ride-through capability of voltage-controlled inverters," *IEEE Trans. Ind. Electron.*, vol. 65, no. 10, pp. 7933–7943, 2018.

[8] X. Guo, W. Liu, and Z. Lu, "Flexible power regulation and current-limited control of the grid-connected inverter under unbalanced grid voltage faults," *IEEE Trans. Ind. Electron.*, vol. 64, no. 9, pp. 7425–7432, 2017.

[9] G. Iwanski, S. Wodyk, and T. Luszczyk, "Control of a three-phase power converter connected to unbalanced power grid in a non-cartesian oblique frame," *IEEE Trans. Power Electron.*, to be published, doi: 10.1109/TPEL.2021.3098697.

[10] S. Affijulla and P. Tripathy, "Development of phasor estimation algorithm for P-class PMU suitable in protection applications," *IEEE Trans. Smart Grid*, vol. 9, no. 2, pp. 1250–1260, 2018.

[11] K. Zhu and P. W. T. Pong, "Fault classification of power distribution cables by detecting decaying DC components with magnetic sensing," *IEEE Trans. Instrum. Meas.*, vol. 69, no. 5, pp. 2016–2027, 2020.

[12] M. Pazoki, "A new DC-offset removal method for distance-relaying application using intrinsic time-scale decomposition," *IEEE Trans. Power Del.*, vol. 33, no. 2, pp. 971–980, 2018.

[13] Z. Jiang, S. Miao, and P. Liu, "A modified empirical mode decomposition filtering-based adaptive phasor estimation algorithm for removal of exponentially decaying DC offset," *IEEE Trans. Power Del.*, vol. 29, no. 3, pp. 1326–1334, 2014.

[14] B. Jafarpisheh, S. M. Madani, and S. Jafarpisheh, "Improved DFT-based phasor estimation algorithm using down-sampling," *IEEE Trans. Power Del.*, vol. 33, no. 6, pp. 3242–3245, Dec. 2018.

[15] D. Celeita, J. D. Perez, and G. Ramos, "Assessment of a decaying dc offset detector on cts measurements applying mathematical morphology," *IEEE Trans. Ind Appl*, vol. 55, no. 1, pp. 248–255, 2019.

[16] U. Subudhi, H. K. Sahoo, and S. K. Mishra, "Harmonics and decaying DC estimation using volterra LMS/F algorithm," *IEEE Trans. Ind Appl*, vol. 54, no. 2, pp. 1108–1118, Mar. 2018.

[17] J. K. Hwang, C. K. Song, and M. G. Jeong, "DFT-based phasor

estimation for removal of the effect of multiple dc components," *IEEE Trans. Power Del.*, vol. 33, no. 6, pp. 2901–2909, 2018.
[18] S. Peyghami, F. Blaabjerg, and P. Palensky, "Incorporating power electronic converters reliability into modern power system reliability analysis," *IEEE J. Emerg. Sel. Topics Power Electron.*, vol. 9, no. 2, pp. 1668–1681, 2021.
[19] K. Fischer, K. Pelka, A. Bartschat *et al.*, "Reliability of power converters in wind turbines: Exploratory analysis of failure and operating data from a worldwide turbine fleet," *IEEE Trans. Power Electron.*, vol. 34, no. 7, pp. 6332–6344, 2019.
[20] A. Sahoo, J. Ravishankar, M. Ciobotaru, and F. Blaabjerg, "Enhanced fault ride-through of power converters using hybrid grid synchronization," *IEEE J. Emerg. Sel. Topics Power Electron.*, to be published, doi: 10.1109/JESTPE.2021.3054851.
[21] W. Freitas, W. Xu, C. Affonso, and Z. Huang, "Comparative analysis between ROCOF and vector surge relays for distributed generation applications," *IEEE Trans. Power Del.*, vol. 20, no. 2, pp. 1315–1324, 2005.
[22] L. Xiong, F. Zhuo, F. Wang *et al.*, "A quantitative evaluation and comparison of harmonic elimination algorithms based on moving average filter and delayed signal cancellation in phase synchronization applications," *J. Power Electron.*, vol. 16, no. 2, pp. 717–730, 2016.
[23] L. Xiong, F. Zhuo, F. Wang *et al.*, "A fast orthogonal signal-generation algorithm characterized by noise immunity and high accuracy for single-phase grid," *IEEE Trans. Power Electron.*, vol. 31, no. 3, pp. 1847–1851, 2016.

Liansong Xiong (Senior Member, IEEE) was born in Guangyuan, Sichuan, China, in 1986. He received the B.S., M.S., and Ph.D. degrees in electrical engineering from Xi'an Jiaotong University (XJTU), Xi'an, China, in 2009, 2012, and 2016, respectively. Since 2014, he has been with the School of E-learning, XJTU, as a part-time *Faculty Member*. In 2016, he joined the School of Automation, Nanjing Institute of Technology (NJIT), Nanjing, China, introduced in High-Level Academic Talent Plan of NJIT. From 2017 to 2019, he joined the Department of Electrical Engineering, The Hong Kong Polytechnic University (PolyU), Hong Kong, as a Research Associate. He is the first author of 14 articles indexed by SCI and more than 20 articles indexed by EI. His current research interests include power quality, multilevel converter, renewable energy generation, and power system stability. He is a *Senior Member* of the IEEE and the China Electrotechnical Society, and a member of the China Power Supply Society (CPSS) and the China Society for Electrical Engineering. He has served as the Guest Associate Editor for the Frontiers in Energy Research, the Program Co-Chair of the 3rd Asia Energy and Electrical Engineering Symposium (AEEES 2021), and the Technical Program Committee Member of IEEE Workshop on Wide Bandgap Power Devices and Applications in Asia (WiPDA-Asia 2018). He received the Best Conference Paper Award once in the international conference and the Excellent Paper Award seven times in domestic conferences. He was honored with the Outstanding Graduates of XJTU in 2015, the First Prize of CPSS Scientific and Technological Progress Award in 2021, the ICPES Young Scientist Award in 2020, the Best Paper Award of Shaanxi Province in 2020, and the Excellent Doctoral Dissertation of XJTU and Shaanxi Province in 2018.

Xiaokang Liu (Member, IEEE) received the Double M.Sc. degrees in electrical engineering from Xi'an Jiaotong University, Xi'an, China, and Politecnico di Milano, Milan, Italy, in 2016, and the Ph.D. degree (summa cum laude) in electrical engineering from Politecnico di Milano, in 2021.

He is currently a Postdoctoral Research Fellow of the Department of Electronics, Information, and Bioengineering, Politecnico di Milano. His research interests include electromagnetic compatibility, power electronics, and signal integrity.

Lei Liu received the B.S. degree from the Hefei University of Technology, Anhui, China, in 2020. He is currently pursuing the master's degree with the School of Electrical Engineering, Xi'an Jiaotong University, China. His current research interests include renewable energy generation and stability analysis.

Yonghui Liu (Student Member, IEEE) received the B.S. degree in electrical engineering from Harbin Institute of Technology, Harbin, China, in 2013 and the M.S. degree in electrical engineering from Xi'an Jiaotong University, Xi'an, China, in 2016. She is currently working toward the Ph.D. degree in electrical engineering in Xi'an Jiaotong University, Xi'an, China. Her research interests include modeling and control of converters, renewable energy integration, VSC-HVDC and wireless power transfer.